Nonlinear Phototaxis and Instabilities in Suspensions of Light-Seeking Algae

Aina Ramamonjy, Julien Dervaux[*], and Philippe Brunet

Laboratoire Matière et Systèmes Complexes, UMR 7057 CNRS and Université de Paris, 75013 Paris, France

The mechanism by which living organisms seek optimal light conditions—phototaxis—is a fundamental process for motile photosynthetic microbes. It is involved in a broad array of natural processes and applications from bloom formation to the production of high-value chemicals in photobioreactors. Here, we show that a population of the model alga *Chlamydomonas reinhardtii* exhibits a highly sensitive nonlinear response to light and demonstrate that the self-organization of cells in a heterogeneous environment becomes unstable as the result of a coupling between bioconvective flows and phototaxis.

Understanding the behavior of semidilute to dense suspensions of active (self-propelled) particles is a central question of contemporary physics at the crossroads of active matter, hydrodynamics, and biophysics [1]. From a theoretical standpoint, much work has been devoted to explain the emergence of collective dynamics in such systems. While individual motions prevail in low-concentration suspensions [2], intercellular interactions become significant when the volume fraction of microbes exceeds a few percent. They generally consists in repulsion or self-alignment and can lead to collective motion such as bacterial turbulence [3,4] or flocking [5] that offers striking similarities with liquid-gas phase transitions. On the experimental side, however, such phenomena have been observed only in highly confined systems [4,6]. In large or unconfined systems, density mismatch between microbes and the carrier fluid drives the emergence of another class of collective effect—bioconvection—characterized by large-scale flows in active suspensions even at a volume fraction below 1% [7–18]. Recently, it has been shown that bioconvection, which also occurs in nature [19], can be triggered and controlled using light beams in suspensions of phototactic microbes that bias their swimming motion in response to light [20–22]. However, the macroscopic modeling of this light-induced directional swimming lacks robust quantitative data, and most studies approximate the phototactic velocity as an on-off function of the local light intensity, apart from rare attempts to introduce more complex effects [16,23–26].

Here, we investigate how a population of the model phototactic alga—*Chlamydomonas reinhardtii* (CR)—moves in heterogeneous luminous landscapes. In the dark, CR swims with a typical velocity $|\vec{u}| \sim 100$ μm/s, and individual cell trajectories can be approximated as long ($\tau \sim 10$ s) straight runs interrupted by short (~ 0.1 s) tumbling events (Fig. 1) [27]. This microscopic dynamics shares many similarities with Brownian motion and implies that the macroscopic cell concentration c of a dilute suspension of microswimmers is well described by a diffusion equation [28]. A concentration gradient $\vec{\nabla}c \neq \vec{0}$ induces a cell flux $D\vec{\nabla}c$, where D is an effective diffusion coefficient that has been measured macroscopically in the range 0.7–0.9×10^{-7} m^2/s [20,27], in agreement with the estimate $D \sim |\vec{u}|^2 \tau$ obtained from the microscopic properties of cells. But how is this dynamics modified in a spatially heterogeneous environment? In particular, how do cells move in a light-intensity gradient? To answer these questions, we first focus on dilute suspensions, where collective effects and bioconvection are negligible.

In order to shape a heterogeneous luminous landscape, a monochromatic (532 nm) light beam of variable width w and maximal intensity $I_{\max}$ was projected onto a Petri dish containing a thin layer (thickness $H \leq 1$ mm) of a dilute, initially homogeneous, CR suspension (Supplemental Material, Fig. S1 [29]). The light intensity $I(r)$ was measured as a function of the distance r from the beam center. Because CR does not respond significantly to wavelengths above ~ 650 nm, a dim homogeneous red light was also projected across the suspension, and the measurement of the transmitted red light intensity was used to obtain, after calibration, the local depth-integrated cell concentration c. Low values of c were chosen to avoid any effect of the cell concentration on the measurements. Following illumination with the inhomogeneous green light, cells accumulate over time in regions of most favorable light intensity until a stationary inhomogeneous concentration field ($\vec{\nabla}c \neq \vec{0}$), sharing the axisymmetry of the light field, is reached [Figs. 1(b)–1(d)]. Several processes occurring at the cellular scale likely contribute to this accumulation; e.g., the light intensity may modulate the swimming velocity, the tumbling frequency, or the tumbling orientation probability distribution. More drastic alteration of the beating patterns such as photophobic or scotophobic shocks may also occur at critical light intensities. In order to obtain a simple yet quantitative description of phototaxis at the population
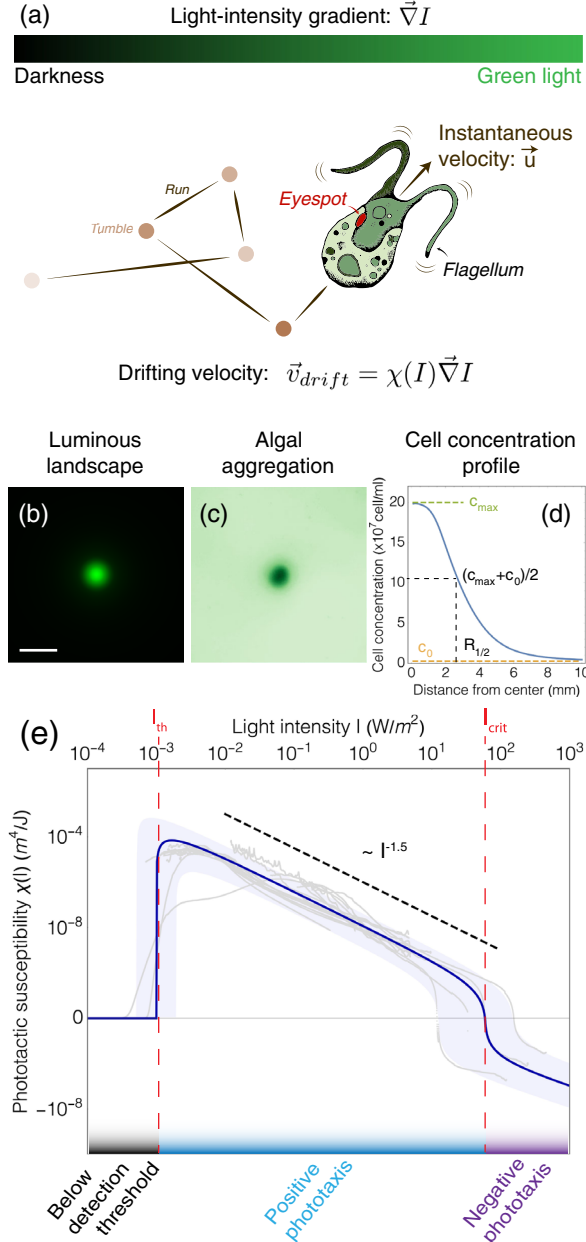
FIG. 1. (a) Cartoon illustrating phototaxis along a light-intensity gradient. The drifting velocity is proportional to the direction and magnitude of the gradient. (b) Typical heterogeneous light field. (c) Stationary accumulation of algae around the beam. Scale bar, 1 cm. (d) Azimuthal average of the stationary concentration field after ~80 min. (e) Bisymmetric logarithmic plot of the phototactic susceptibility $\chi(I)$ as a function of I. The graph is obtained by plotting $\text{sgn}(\chi) \log(1 + |\chi|/c)$ versus $\log I$. $c = 10^{-12}$ m^4/J is an arbitrary constant that removes the singularity near $\chi = 0$. Gray lines, individual experiments. Blue line, function (1) using the values in Table I.

scale, we do not model each of these mechanisms but use a Keller-Segel approach instead [30]. In this framework, the nonzero diffusive flux $D\vec{\nabla}c$ arising from an inhomogeneous concentration is balanced by a phototactic flux $c\vec{v}_{\text{drift}}$ in the

stationary state. In the simplest approximation, the drift velocity $\vec{v}_{\text{drift}}$ is proportional to the light-intensity gradient $\vec{\nabla}I$, and, thus, $\vec{v}_{\text{drift}} = \chi(I)\vec{\nabla}I$. Although an additional drift velocity along the direction of light propagation (orthogonal to the free surface of the suspension) could also be involved, it is largely subdominant here [20] and is neglected. The proportionality coefficient $\chi(I)$ is a photo-tactic susceptibility quantifying the propensity of cells to migrate in a light-intensity gradient and encompasses all the microscopic mechanisms involved during phototaxis. The axisymmetric stationary solution reads $\chi(r) = \{D[(\partial c)/(\partial r))]\}/[c[(\partial I)/(\partial r)]]$. $\chi(r)$ is space-dependent, because $I(r)$ varies spatially: $\chi(r) \equiv \chi[I(r)]$.

Several experiments at various maximal intensities ($I_{\text{max}} \in [1\text{--}500]$ W/m^2), beam widths, and cell concentration were carried out, and the phototactic susceptibility $\chi(r)$ was measured in the stationary states. The parametric curves $\{I(r), \chi(r)\}$ obtained from each experiment were plotted together. They indeed collapsed to yield a χ versus I master curve spanning seven decades in light intensity and shown as a bisymmetric log-log plot in Fig. 1(e). These experimental data reveal that the phototactic susceptibility is a highly nonlinear function of I, and, despite the dispersion, three qualitatively different regimes can clearly be identified: (i) no phototactic response ($\chi \approx 0$) below a detection threshold I_{th}, (ii) positive phototaxis ($\chi > 0$) with a power-law decrease over ~4 decades at intermediate I, and (iii) negative phototaxis ($\chi < 0$) above a critical intensity I_{crit}. For practical purposes, the phototactic susceptibility is approximated by the function:

$$\chi(I) = \begin{cases} 0, & I < I_{\text{th}}, \\ \alpha_p \dfrac{(1-\frac{I}{I_{\text{crit}}})(\frac{I}{I_{\text{th}}}-1)}{(\frac{I}{I_{\text{crit}}})^{1+m}}, & I_{\text{th}} < I < I_{\text{crit}}, \\ \alpha_n\left(1 - \dfrac{I}{I_{\text{crit}}}\right), & I_{\text{crit}} < I. \end{cases} \quad (1)$$

Best-fitted values of the parameters in Eq. (1) are summarized in Table I. Note that a detection threshold intensity of $I_{\text{th}} \sim 1$ mW/m^2 at 532 nm corresponds to a photon flux density of 3×10^{15} photons/(m^2 s). Given that the number of Channelrhodopsins is ~30 000 per cell [31,32], with an absorption cross section of 1.5×10^{-20} m^2 per rhodopsin and a photochemical quantum efficiency of 0.67 [33], we deduce that I_{th} corresponds to the detection of ~1 photon per second per cell. Since the photo-current induced by the photoisomerization of the rhodopsin reaches a peak within milliseconds [34], much faster than 1 s, we deduce that a single photon absorption event is sufficient to trigger phototaxis in a cell. This high sensitivity is in agreement with previous electrophysiology measurements performed at the cellular scale [35], but here measured noninvasively at the population scale. At the critical intensity $I_{\text{crit}} \sim 100$ W/m^2, where phototaxis switches from positive to negative, ~80 000

TABLE I. Parameters for the phototactic function $\chi(I)$.

Symbol	Meaning	Value range
I_{th}	Detection threshold intensity	$1.2 \pm 0.7 \times 10^{-3}$ W/m^2
I_{crit}	Critical intensity separating positive and negative phototaxis	101 ± 81 W/m^2
m	Power-law exponent	1.5 ± 0.2
α_p	Positive phototaxis strength	$8 \pm 5 \times 10^{-17}$ m^4/J
α_n	Negative phototaxis strength	$4 \pm 2 \times 10^{-11}$ m^4/J

photoisomerization events occur per cell every second. Under continuous light conditions, the open state of the Channelrhodopsin has a relaxation timescale of 250 ms to the dark-adapted state [36], indicating that a Channelrhodopsin molecule may be photoisomerized ∼4 times every second. We conclude that ∼2/3 of the rhodopsin molecules in the cell are photoisomerized at I_{crit} and that a broad range of photoisomerization states, from single molecule activation to almost full continuous activation of all photoreceptors, is used in the positive phototaxis regime. Although it endows CR phototaxis with a remarkable dynamic range, it leaves open the question of the molecular mechanisms controlling CR photophobic response, since most Channelrhodopsin are already activated at I_{crit}. Recent experiments suggest that Channelrhodopsin dephosphorylation at high light intensity might be involved [37]. Finally, we note that the I-average value of χ in the positive phototaxis regime (for $I_{th} < I < I_{crit}$) is ∼2×10^{-7} m^4/J, very close to our previous estimate [using a constant χ to fit $c(r)$ profiles [20]].

Having established a connection between the subcellular processes underlying phototaxis and the macroscopic behavior of a dilute algal population, we now investigate the emergence of collective behavior in semidilute suspensions. Because of the density mismatch $\Delta\rho$ between CR and the carrier fluid ($\Delta\rho \sim 50$ kg/m^3), algae-rich regions are denser than algae-poor regions. This density gradient induces a pressure gradient in the active suspension which generate macroscopic, *bioconvective*, fluid flows [7–18,20–22]. Their magnitude is controlled by the pseudo-Rayleigh number

$$\mathrm{Ra} = \frac{H^3 \Delta\rho g c_0}{D\nu}, \qquad (2)$$

where H is the suspension depth, g is the gravity constant, c_0 is the initial homogeneous cell concentration, and ν is the fluid kinematic viscosity, supposedly independent on c_0. Experimentally, Ra was varied by tuning c_0 and H. The maximum light intensity was fixed at 5 W/m^2, and the beam width w was in the range [2.7–20] mm. We monitored the algal aggregation process as a function of Ra and of the magnitude of the light-intensity gradient, the latter being tuned by varying w (Supplemental Material, Figs. S2 and S3 [29]). We first observed that the maximum

dimensionless concentration c_{max}/c_0 was weakly dependent on Ra for values up to ∼100 before decreasing strongly for higher Ra [Fig. 2(a)]. Because the measurements to extract $\chi(I)$ presented above were conducted for Ra ∼ 10, this observation confirms that they were indeed performed in a regime independent of the cell concentration. While no significant effect of the beam width w on c_{max}/c_0 was observed, the pattern width $R_{1/2}$, on the other hand, was found to increase with both w and Ra [Fig. 2(b)]. Depending on the value of the control parameters, the cell population self-organizes into distinct patterns whose distribution in the parameter space is represented in Fig. 2(c). At low relative beam width and pseudo-Rayleigh number, stationary *round* patterns are observed. They follow closely the light beam. As we already shown in a previous work [20], when the pseudo-Rayleigh number is increased at low w/H, circular *waves* of concentrated algae are emitted periodically. At a larger relative beam width w/H, a very different short wavelength instability is found above a critical threshold in Rayleigh number. In this *dendrite instability*, orthoradial invariance is lost but stationarity is retained. These patterns consist of periodic thin dendrites that grow radially and exhibit splitting [Fig. 2(d)] until a final state is reached. Dendrite patterns appear in the same range of Ra as radial waves (Ra ≳ 100) but with a strong dependance on w. Since the primary flow is radial, circular waves are advected while dendrites remain stationary. The dimensionless wavelength λ/H is 0.63 ± 0.08, roughly independent of Ra [Fig. 2(e)]. Finally, at intermediate Ra and large enough w/H ratio, a *budding instability* is observed. In this regime, a budlike structure grows from the circular cell aggregate. We also observed a *mixed dendrite and bud* state in which both the growth of the bud as well as the dendrite instability occurred simultaneously. It was previously suggested that gyrotaxis could trigger radial waves [20]. Hereafter, we present a semiquantitative model suggesting gyrotaxis can also induce the orthoradial dendrites. We introduce an anisotropic nonlinear diffusion-drift equation for the depth-averaged dimensionless cell concentration field $c(r, \theta, t)$:

$$\frac{1}{D}\frac{\partial c}{\partial t} = \vec{\nabla} \cdot \left\{ \mathbf{\Lambda}(c)\vec{\nabla}c - c\frac{\chi(r)}{D}\vec{\nabla}I \right\}. \qquad (3)$$

The initial condition is $c(r, \theta, t = 0) = 1$, while the radial component of the mass flux $\{\mathbf{\Lambda}\vec{\nabla}c - [c\chi(r)/D]\vec{\nabla}I\} \cdot \vec{e}_r = 0$ at the outer boundary $r = L$. The second term in the rhs of Eq. (3) describes phototaxis toward the beam center. The nonlinear anisotropic diffusion matrix $\mathbf{\Lambda}(c)$ can be represented in the base $(\vec{e}_r, \vec{e}_\theta)$ as the sum of three terms of distinct physical origins:

$$\mathbf{\Lambda} = \underbrace{\begin{pmatrix} 1 & 0 \\ 0 & 1 \end{pmatrix}}_{\text{diffusion}} + \underbrace{\begin{pmatrix} \alpha\mathrm{Ra}c & 0 \\ 0 & \alpha\mathrm{Ra}c \end{pmatrix}}_{\text{convection}} + \underbrace{\begin{pmatrix} 0 & 0 \\ 0 & -\gamma\mathrm{Ra}c \end{pmatrix}}_{\text{gyrotaxis}}.$$
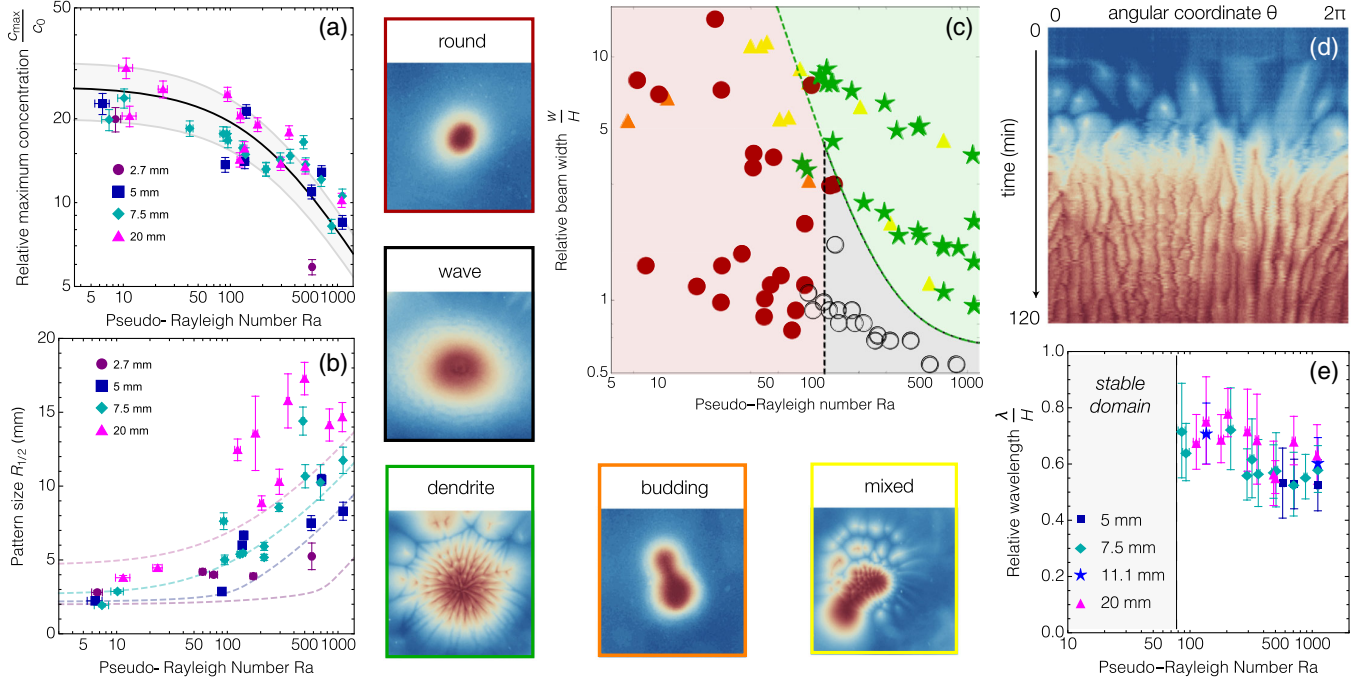
FIG. 2. (a) Log-log plot of $c_{\max}/c_0$ versus Ra for several w. Black line, theoretical prediction [$A = 26 \pm 6$ and $\alpha = (1.5 \pm 0.3) \times 10^{-4}$]. Gray area, corresponding error interval. (b) Log-lin plot of the pattern radius $R_{1/2}$ versus Ra for several w. Dotted colored lines, theoretical predictions. (c) Phase diagram showing the distribution of instabilities as a function of Ra and w/H. Pictures show typical patterns (high concentrations in red and low concentrations in blue). (d) Kymograph of the normalized cell concentration, 5 mm from the beam center, as a function of the angular coordinate and time, showing dendrite splitting and merging. (e) Lin-log plot of the dimensionless wavelength λ/H versus Ra for different w.

The first term in the rhs accounts for the run-and-tumble motion of the cells. The second term, nonlinear, represents algal advection by bioconvection and is proportional to Ra. The third term stems from the gyrotaxis of the algae: Their orientation is affected by the flow-induced viscous torque [8–10,13,14,17,18,20]. It depends on the magnitude of the flow through Ra and on the gyrotactic properties of algae through γ. This term applies only in the orthoradial direction, since gyrotaxis is directed in the direction orthoradial to the primary fluid flow which is mostly radial. Experimentally, γ could be measured by using an asymmetrical beam and fitting the concentration profiles with Eq. (3). While the nonlinear equation (3) can be derived by a dimensionality reduction of a general 3D model of bioconvection, as will be presented in a subsequent study, it is used here as a phenomenological model to capture some of the experimental features. Equation (3) has a stationary axisymmetric solution $c_{\mathrm{eq}}(r)/c_0 = \mathcal{W}(A\alpha\mathrm{Ra}e^{\int_0^r \{[\chi(r)]/D\}[(\partial I)/(\partial r)dr]})/(\alpha Ra)$, where $\mathcal{W}(y)$ is the Lambert function. The constant A is deduced from the global cell conservation. Since $c_{\mathrm{eq}}(r)$ decreases monotonically with r in the positive phototaxis regime, the maximum concentration $c_{\max} = c_{\mathrm{eq}}(r=0)$ is reached at $r=0$ and is independent of w. Noting the asymptotic expansion $\mathcal{W}(y) \underset{y \ll 1}{\sim} y$, we have $c_{\max}/c_0 \approx A$ for Ra $\to 0$ and, thus, A is physically the maximum concentration

factor. The dimensionless parameter $\alpha = (1.5 \pm 0.3) \times 10^{-4}$ quantifies the efficiency of the convective process to transport algae away from the concentrated region. It is found by fitting the experimental data for $c_{\max}/c_0$ with the model [Fig. 2(a)]. Once fully constrained, the model reproduces reasonably well the dependence of the pattern size on both w and Ra [Fig. 2(b)]. In particular, the nonlinear phototactic response (1) is critical to predict the concentration profiles (Supplemental Material, Fig. S4 [29]). Going further, we note that, provided $\gamma > \alpha$, the orthoradial component of the diffusion tensor $[1 + (\alpha - \gamma)\mathrm{Ra}c]$ becomes negative when the product $\mathrm{Ra}c$ becomes large enough. Since a negative diffusion coefficient is associated with a short wavelength instability, akin to the spinodal instability of the Cahn-Hilliard equation, the model predicts that a short wavelength orthoradial instability occurs when Ra exceeds a threshold value, as observed experimentally. The selection of the instability wavelength likely results from small-scale mechanisms not included in Eq. (3).

Although still poorly quantified for most microbial species beyond the cellular scale, phototaxis is of major importance for the understanding of fundamental problems in ecology such as the diel migration of the phytoplankton [38] or blooms [39,40]. From an applied standpoint, it may also contribute to biomass growth optimization in photobioreactors. With these considerations in mind, we have

developed an experimental setup enabling a convenient quantification of the phototactic response of swimming microorganisms at the population scale, relevant to a broad range of applications. We have shown that CR exhibits a highly nonlinear phototactic response over 7 orders of magnitude in light intensity and introduced a phenomenological law to describe this response. We have uncovered a detection threshold, a critical intensity driving the switch from positive to negative phototaxis, and we have established a link between these quantities, measured at the population scale, and subcellular processes. In a second step, we have investigated how a cell population self-organizes in a heterogeneous light field as a function of the strength of the collective effects, here controlled through the pseudo-Rayleigh number Ra. We found that the interplay between nonlinear phototaxis and bioconvection leads to remarkable symmetry-breaking instabilities that we partly reproduce in a simplified theoretical model. Beside exhibiting very rich patterns that should inspire the development of refined models in nonlinear and active matter physics, we anticipate that the nonlinear phototactic response uncovered in this study, coupled to self-generated bioconvective flows, will enable a fine control over the spatial organization of microbial populations that will help in the development of efficient strategies for the harvesting or biomixing of microbes in photobioreactors.

---

*Corresponding author.
 julien.dervaux@univ-paris-diderot.fr

[1] M. C. Marchetti, J. F. Joanny, S. Ramaswamy, T. B. Liverpool, J. Prost, M. Rao, and R. A. Simha, Rev. Mod. Phys. **85**, 1143 (2013).

[2] E. Lauga and T. R. Powers, Rep. Prog. Phys. **72**, 096601 (2009).

[3] L. Dombrowski, L. Cisneros, S. Chatkaew, R. E. Goldstein, and J. O. Kessler, Phys. Rev. Lett. **93**, 098103 (2004).

[4] J. Dunkel, S. Heidenreich, K. Drescher, H. H. Wensink, M. Bär, and R. E. Goldstein, Phys. Rev. Lett. **110**, 228102 (2013).

[5] A. Bricard, J. B. Caussin, N. Desreumaux, O. Dauchot, and D. Bartolo, Nature (London) **503**, 95 (2013).

[6] L. Cisneros, J. Kessler, S. Ganguly, and R. Goldstein, Phys. Rev. E **83**, 061907 (2011).

[7] S. Childress, M. Levandowksy, and E. A. Spiegel, J. Fluid Mech. **69**, 591 (1975).

[8] J. O. Kessler, Nature (London) **313**, 218 (1985).

[9] T. J. Pedley, N. A. Hill, and J. O. Kessler, J. Fluid Mech. **195**, 223 (1988).

[10] N. A. Hill, T. J. Pedley, and J. O. Kessler, J. Fluid Mech. **208**, 509 (1989).

[11] T. J. Pedley and J. O. Kessler, Annu. Rev. Fluid Mech. **24**, 313 (1992).

[12] R. Vincent and N. Hill, J. Fluid Mech. **327**, 343 (1996).

[13] M. A. Bees and N. A. Hill, J. Exp. Biol. **200**, 1515 (1997).

[14] M. A. Bees and N. A. Hill, Phys. Fluids **10**, 1864 (1998).

[15] I. M. Janosi, J. O. Kessler, and V. K. Horvath, Phys. Rev. E **58**, 4793 (1998).

[16] S. Ghorai and N. A. Hill, Phys. Fluids **19**, 054107 (2007).

[17] C. R. Williams and M. A. Bees, J. Exp. Biol. **214**, 2398 (2011).

[18] C. R. Williams and M. A. Bees, J. Fluid Mech. **678**, 41 (2011).

[19] T. Sommer, F. Danza, J. Berg, A. Sengupta, G. Constantinescu, T. Tokyay, H. Brgmann, Y. Dressler, O. Sepulveda Steiner, C. J. Schubert, M. Tonolla, and A. Wuest, Geophys. Res. Lett. **44**, 9424 (2017).

[20] J. Dervaux, M. Capellazzi Resta, and P. Brunet, Nat. Phys. **13**, 306 (2017).

[21] J. Arrieta, M. Polin, R. Saleta-Piersanti, and I. Tuval, Phys. Rev. Lett. **123**, 158101 (2019).

[22] A. Javadi, J. Arrieta, I. Tuval, and M. Polin, Phil. Trans. R. Soc. A **378**, 20190523 (2020).

[23] A. Giometto, F. Altermatt, A. Maritan, R. Stocker, and A. Rinaldo, Proc. Natl. Acad. Sci. U.S.A. **112**, 7045 (2015).

[24] K. Leptos, M. Chioccioli, S. Furlan, A. Pesci, and R. Goldstein, An adaptive flagellar photoresponse determines the dynamics of accurate phototactic steering in Chlamydomonas, BioRxiv (2018), pp. 254714.

[25] J. Arrieta, A. Barreira, M. Chioccioli, M. Polin, and I. Tuval, Sci. Rep. **7**, 1 (2017).

[26] S. Choudhary, A. Baskaran, and P. Sharma, Biophys. J. **117**, 1508 (2019).

[27] M. Polin, I. Tuval, K. Drescher, J. P. Gollub, and R. E. Goldstein, Science **325**, 487 (2009).

[28] H. Othmer, S. Dunbar, and W. Alt, J. Math. Biol. **26**, 263 (1988).

[29] See Supplemental Material at http://link.aps.org/supplemental/10.1103/PhysRevLett.128.258101 for details on the experimental setup and additional data analysis.

[30] E. Keller and L. Segel, J. Theor. Biol. **30**, 225 (1971).

[31] K. W. Foster and R. D. Smyth, Microbiol. Rev. **44**, 572 (1980).

[32] W. Deininger, P. Kröger, U. Hegemann, F. Lottspeich, and P. Hegemann, EMBO J. **14**, 5849 (1995).

[33] K. W. Foster, J. Saranak, N. Patel, G. Zarilli, M. Okabe, T. Kline, and K. Nakanishi, Nature (London) **311**, 756 (1984).

[34] H. Harz and P. Hegemann, Nature (London) **351**, 489 (1991).

[35] K. Schaller, R. David, and R. Uhl, Biophys. J. **73**, 1562 (1997).

[36] J. Kuhne, J. Vierock, S. A. Tennigkeit, M.-A. Dreier, J. Wietek, D. Petersen, K. Gavriljuk, S. F. El-Mashtoly, P. Hegemann, and K. Gerwert, Proc. Natl. Acad. Sci. U.S.A. **116**, 9380 (2019).

[37] M. Böhm, D. Boness, E. Fantisch, H. Erhard, J. Frauenholz, Z. Kowalzyk, N. Marcinkowski, S. Kateriya, P. Hegemann, and G. Kreimer, Plant Cell **31**, 886 (2019).

[38] G. Jékely, J. Colombelli, H. Hausen, K. Guy, E. Stelzer, F. Nédélec, and D. Arendt, Nature (London) **456**, 395 (2008).

[39] T. J. Smayda, Limnol. Oceanogr. **42**, 1137 (1997).

[40] J. Dervaux, A. Mejean, and P. Brunet, PLoS One **10**, e0120906 (2015).